Actively crosslinked microtubule networks: mechanics, dynamics and filament sliding

Sebastian Fürthauer,[1] Bezia Lemma,[2,3,4] Peter J. Foster,[5] Stephanie C. Ems-McClung,[6] Claire E. Walczak,[6] Zvonimir Dogic,[3,4] Daniel J. Needleman,[7] and Michael J. Shelley[1,8]

[1]*Center for Computational Biology, Flatiron Institute, New York, NY 10010, USA*
[2]*Department of Physics, Harvard University, Cambridge, MA 02138, USA*
[3]*Department of Physics, Brandeis University, Waltham, MA 02454, USA*
[4]*Department of Physics, University of California, Santa Barbara, CA 93106, USA*
[5]*Physics of Livings Systems, Department of Physics, Massachusetts Institute of Technology, Cambridge, MA 02139, USA*
[6]*Medical Sciences Program, Indiana University, Bloomington, IN 47405, USA*
[7]*Paulson School of Engineering & Applied Science and Department of Molecular & Cellular Biology, Harvard University, Cambridge, MA 02138, USA*
[8]*Courant Institute, New York University, New York, NY 10012, USA*

arXiv:1812.01079v1 [cond-mat.soft] 3 Dec 2018

Cytoskeletal networks are foundational examples of active matter and central to self-organized structures in the cell. *In vivo*, these networks are active and heavily crosslinked. Relating their large-scale dynamics to properties of their constituents remains an unsolved problem. Here we study an *in vitro* system made from microtubules and XCTK2 kinesin motors, which forms an aligned and active gel. Using photobleaching we demonstrate that the gel's aligned microtubules, driven by motors, continually slide past each other at a speed independent of the local polarity. This phenomenon is also observed, and remains unexplained, in spindles. We derive a general framework for coarse graining microtubule gels crosslinked by molecular motors from microscopic considerations. Using the microtubule-microtubule coupling, and force-velocity relationship for kinesin, this theory naturally explains the experimental results: motors generate an active strain-rate in regions of changing polarity, which allows microtubules of opposite polarities to slide past each other without stressing the material.

Active materials are made from energy consuming constituents whose activity keeps the system out of equilibrium. Their study has deepened our understanding of self-organizing processes, both *in vivo* and *in vitro* [1, 2]. Its foundational examples include suspensions of microswimmers, *in vitro* assemblies of purified cellular components, and the cell cytoskeleton [3]. While notable progress has been made in deciphering the non-equilibrium physics of active materials by using experiments and symmetry-based phenomenological theories [4–6], there is far less understanding of how the large-scale dynamics actually devolves from microscopic activity. Having such theoretical frameworks would be powerful, allowing the development of unified analysis and design tools for new active materials, and understanding the biology of the cell cytoskeleton. Here we address this challenge for systems made of cytoskeletal polymers which are fully percolated by moving molecular motors. First, we report observations of a dense nematically-aligned active gel made from purified microtubules and XCTK2 kinesin motors. Driven by these motors, its microtubules continually slide within the gel. Using photo bleaching we show the surprising result that their sliding speed is independent of the local gel polarity. This independence of speed from polarity is also observed in *Xenopus* meiotic spindles [7–9] and is an unexplained feature that suggests an robust internal coupling of the microtubular material. To investigate this phenomenon, we introduce a framework for deriving continuum theories for heavily crosslinked, active gels from microscopic considerations. We use this framework to obtain a theory for the XCTK2-microtubule system which explains our experimental findings without adjustable parameters.

How large-scale behaviors of actively crosslinked networks emerge from the properties of their constituents is an actively researched topic in biology [10, 11]. Many aspects of cell biology, including cell shape, motility, and division, are driven by the cytoskeleton [12]. The cytoskeleton consists of polar filaments - mainly actin and microtubules - and the proteins which crosslink them and organize their behavior. Molecular motors are active crosslinkers that use chemical energy to move filaments relative to each other. They play a central role in determining the architecture and dynamics of cytoskeletal structures such as the cell cortex and the spindle [3]. The XCTK2-microtubule system we present here recapitulates the previously unexplained polarity independent sliding motion of microtubules that was observed using speckle microscopy in *Xenopus* meiotic spindles [7–9] and allows us to study how polarity independent filament motion can emerge in actively crosslinked networks.

Phenomenological theories for actively crosslinked networks [1, 4–6, 13] have been derived from conservation laws and symmetry considerations. They can reproduce the pattern of flows observed in artificial [14] and biological systems such as the cell cortex [10, 15–17] and quantitatively explain some aspects of spindle structure and dynamics [18]. However, such theories do not address how the large-scale behaviors of actively crosslinked networks emerge from the properties of its constituents. For

this, an approach that derives macroscopic material laws from the properties of motors and filaments is needed.

Previous efforts to derive continuum theories for active gels from microscopic interactions [19–29] have considered dilute systems, in which individual motor-filament clusters are thought of as disconnected objects. In contrast, actively crosslinked networks, such as the cytoskeleton[3, 30] are crosslinked over scales comparable to the system size and display behaviors different from those predicted by a dilute theory.

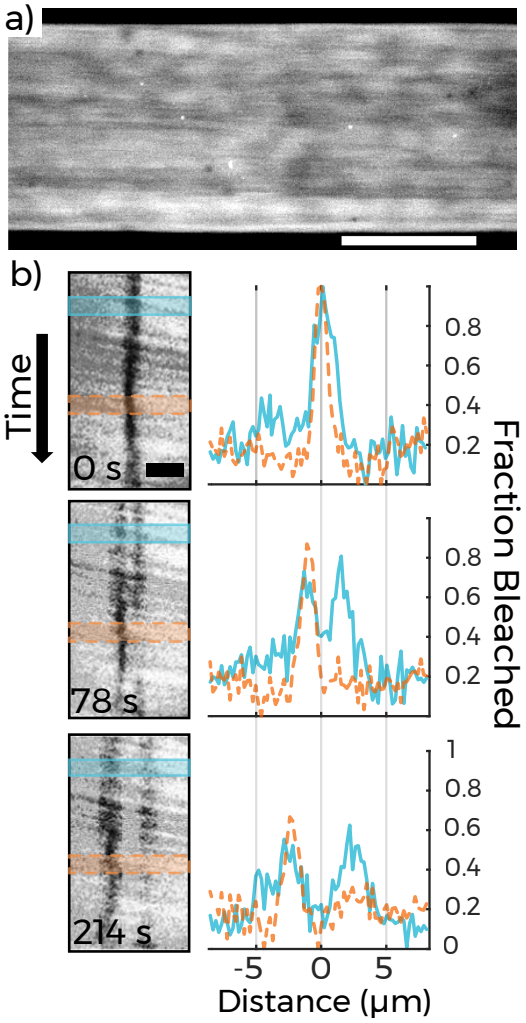


FIG. 1: Bleaching experiments on an aligned gel of stabilized microtubules and XCTK2 molecular motors. (a): An image of the aligned gel within a microfluidic chamber. 50μm scale bar. (b): (left) Higher magnification image of a bleached line within the above material. 5μm scale bar. The bleached line splits into two parallel lines as the microtubules slide apart. (right) Line scans of the bleached image highlighting a region of high polarity (orange, dotted line, $P_{exp} = 0.63 \pm 0.12$) and a neighboring region of low polarity (blue, solid line, $P_{exp} = 0.08 \pm 0.17$) While the polarity of these two regions greatly differs, the peaks move apart at nearly identical speeds.

Experiments: To study the behavior of heavily crosslinked active gels we created one using a *in vitro* system of purified components. We made solutions of fluorescently labeled tubulin and fluorescently labeled XCTK2, a Kinesin-14 molecular motor capable of crosslinking and sliding aligned microtubules [31]. We added paclitaxel to the solution, which nucleates and stabilizes microtubules, and rapidly loaded the sample into a rectangular microfluidic chamber (see Methods for details).

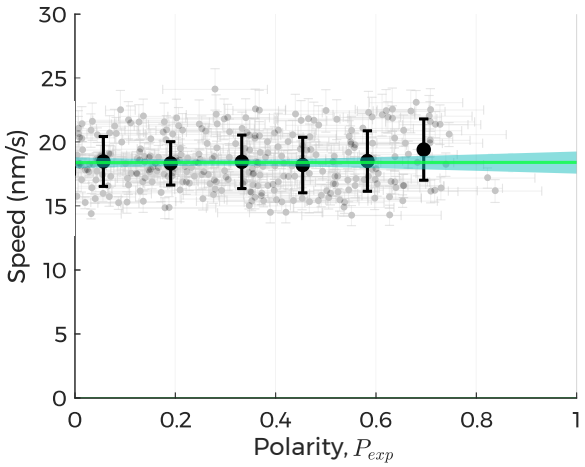


FIG. 2: Sliding speed *vs.* polarity from photobleaching experiments. Each gray dot corresponds to a local measurement of sliding speed and polarity from a bleach line, as in Fig. 1 ($n = 413$). Error bars in the individual velocities correspond to 95% confidence intervals of a linear regression of positions of the bleached line over time. Error bars in the individual polarities correspond to the standard deviation of the local polarity over time. Large black dots show measurements binned by polarity with error bars showing the corresponding standard deviation. In solid green is a regression line, and shaded behind it is the 95% confidence interval of predicted responses to the regression. The Pearson correlation coefficient is 0.08 with the 95% confidence bounds between −0.08 and 0.15 (not significantly different from 0, p-value= 0.51).

The microtubule-motor mixture spontaneously self-organizes into a macroscopic gel, in which microtubules are nematically aligned parallel to the long axis of the microfluidic chamber (Fig. 1A). Once the microtubules are aligned they display continuous polar motion, sliding along the materials director axis. The activity of the gel results in a buckling instability on time scales much longer than those considered here.

We observe this material motion parallel to the director by photo-bleaching the microtubules. As bleaching marks only a subset of microtubules, it allows their subsequent motions to be monitored. We used a femtosecond Ti:Sapphire laser to bleach lines orthogonal to the direction of nematic alignment. Control experiments confirmed that the laser bleached, but did not ablate, the microtubules (see Methods). The bleached material

splits into two parallel lines which move apart along the direction of alignment (Fig. 1B,left), indicating that microtubules in the gel are continually sliding relative to each other.

When a bleached line splits into two, the relative fluorescent intensity of the two new lines reflects the relative number of left-moving and right-moving microtubules. Hence the relative bleach intensity provides a measure of the polarity at the location of the bleach. We define experimental polarity as $P_{exp} = |\frac{A_1 - A_2}{A_1 + A_2}|$, where A_1 and A_2 are the amplitudes of bleach intensities of the two lines. The speed at which the two new lines move apart provides a measure of the speed of microtubule sliding. Along the same bleach line, some regions have very high polarity (Fig. 1B, orange, $P_{exp} = 0.63 \pm 0.12$), while others have very low polarity (Fig. 1B, blue, $P_{exp} = 0.08 \pm 0.17$).

Despite differences in polarity, the speed of bleach line remains fairly constant, (see Fig. 2). This result argues that the microtubule sliding speed has little to no dependence on polarity in these gels. This is similar to the independence of microtubule sliding speed and polarity observed in spindles [7–9], where they have been quantified using speckle microscopy. Bleach lines in these gels with XCTK2 move apart at an average speed of 18.6 ± 0.9nm/s, very close to the observed speed of ~ 20nm/s that XCTK2 slides apart isolated pairs of microtubules [31].

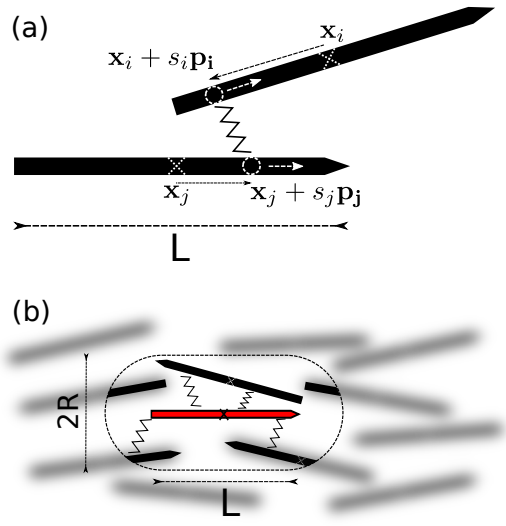


FIG. 3: Sketch of the microscopic model: (a) each microtubule (black solid arrow) is characterized by its center of mass position $\mathbf{x}$ (white crosses) and its orientation $\mathbf{p}$. Microtubules interact via motor molecules (zig-zag line) which connect them at positions s_i, s_j (white circles) on and walk towards their plus ends (white arrows). (b) In the gel crosslinkers of a test-microtubule (red) explore all possible connections to other microtubules within reach (within the dashed capsule), i.e within a sphere of radius R around any position along the test-microtubule.

The polarity independent sliding speed of microtubules is difficult to reconcile with current theories of cytoskeletal filaments and molecular motors. These theories apply in the case of dilute and sparsely crosslinked networks, in which the length scale over which filaments are crosslinked is small compared to the system size. To elucidate the issue, we follow the arguments presented in [19, 27] which consider a dilute collection of sharply aligned microtubules interacting via molecular motors. In the absence of external driving forces, balance of forces yields $\rho^+ f^+ + \rho^- f^- = 0$, where $\rho^\pm$ are the densities of microtubules pointing along the nematic axis of the system in the positive and negative directions, respectively, and $f^\pm$ are the forces acting on microtubules from their interactions with $\mp$ microtubules, respectively. In a dilute system the force exerted by a motor on a microtubule is balanced only by the drag between the microtubule and the surrounding medium and, assuming the medium is locally at rest, the velocity on microtubules $v^\pm$ will be given by $v^\pm = \mu f^\pm$, where μ is the microtubule-mobility. If the molecular motor crosslinking the microtubules moves at a speed V, this imposes $v^+ - v^- = 2V$. Taken together, this leads to $v^\pm = \mp V(1 \mp P)$, where $P = \frac{\rho^+ - \rho^-}{\rho^+ + \rho^-}$ is the polarity.

That is, the sliding velocity of microtubules is predicted to vary linearly with polarity, in conflict with what is observed in our experiments as well as in spindles. Fundamentally, this result is a consequence of force balance in dilute systems: the mass fluxes of left moving and right moving microtubules locally balance. This generalizes to more sophisticated versions of dilute theories that include additional effects, such as long-range hydrodynamics. The disagreement between this theory and experiment suggests that this system may not be in a dilute regime. In order to probe this possibility, we quantified the microtubule density in our gel by measuring the initial molarity of components in our mixture and then determined the percentage of those components which were incorporated into the final gel via fluorescence microscopy. We estimate a 5% volume fraction of polymerized microtubules in the gels, with 17 microtubules per μm^3 (See Methods) and $\sim$ 25 XCTK2 dimers bound to each microtubule. Since microtubules are significantly longer than their average spacing, this result argues that these networks are dense and heavily crosslinked by molecular motors–far from the dilute theory described above. Thus, we introduce a theory of heavily crosslinked networks of microtubules and molecular motors.

Theory for a heavily crosslinked microtubule gel. In our theory, microtubules are characterized by their length L, and their velocities $\mathbf{v}_i$ and orientations $\mathbf{p}_i$. Generically the distribution of microtubules $\psi(\mathbf{x}, \mathbf{p}) = \sum_i \delta(\mathbf{x} - \mathbf{x}_i)\delta(\mathbf{p} - \mathbf{p}_i)$ obeys the Smoluchowski equation $\partial_t \psi = -\nabla(\dot{\mathbf{x}}\psi) - \partial_{\mathbf{p}}(\dot{\mathbf{p}}\psi)$. The microtubules transla-

tional $\dot{\mathbf{x}}(\mathbf{x}_i, \mathbf{p}_i) = \mathbf{v}_i$ and rotational $\dot{\mathbf{p}}(\mathbf{x}_i, \mathbf{p}_i) = \dot{\mathbf{p}}_i$ fluxes can be determined from the force balance $\mathbf{F}_i = 0$ and torque balance $\mathbf{T}_i = 0$ conditions which state that the total force $\mathbf{F}_i$ and torque $\mathbf{T}_i$ on each microtubule vanish.

The forces and torques applied to microtubules are generated by molecular motors which actively crosslink them. Here, motors are characterized by their force-velocity relation, the distance R (the motor size) over which they can crosslink filaments, and the crosslinking torque that they apply. The force that microtubule j exerts on microtubule i, via active crosslinks between $\mathbf{x}_i + s_i\mathbf{p}_i$ and $\mathbf{x}_j + s_j\mathbf{p}_j$ (see Fig. 3a), is given by $\mathbf{F}_{ij}$ and the total force on microtubule i is

$$\mathbf{F}_i = \int_{-L/2}^{L/2} ds_i \sum_j \int_{-L/2}^{L/2} ds_j \int d\mathbf{p}_j \int_{\Omega(\mathbf{x}_i+s_i\mathbf{p}_i)} dx^3 \times\delta(\mathbf{x} - \mathbf{x}_j - s_j\mathbf{p}_j)\delta(\mathbf{p} - \mathbf{p}_j)\mathbf{F}_{ij}, \quad (1)$$

where $\Omega(\mathbf{x})$ denotes a sphere of radius R centered at $\mathbf{x}$ (see Fig. 3b). We note that the force density can be written as the divergence of the network stress tensor $\mathbf{\Sigma}$ according to Kirkwood's formula since $\mathbf{F}_{ij} = -\mathbf{F}_{ji}$. Thus, the force balance of the network reads

$$\nabla \cdot \mathbf{\Sigma}(\mathbf{x}) = \sum_i \mathbf{F}_i \delta(\mathbf{x} - \mathbf{x}_i) = \mathbf{0}. \quad (2)$$

The torque that a crosslinker between filaments i and j exerts on filament i is given by $\mathbf{T}_{ij} = s_i\mathbf{p}_i \times \mathbf{F}_{ij} + \mathbf{\Gamma}_{ij}$, a where $\mathbf{\Gamma}_{ij}$ is the contribution stemming from an explicit crosslinker torque. The total torque $\mathbf{T}_i$ on microtubule i obeys an equation analogous to Eq. (1), (see Methods).

We model the XCTK2 motors by a force-velocity relation $\mathbf{F}_{ij}(\Delta\mathbf{v}_{ij})$, which depends on the velocity difference $\Delta\mathbf{v}_{ij}$ between the attachment points of the motor on the two microtubules, and a crosslinking torque $\mathbf{\Gamma}_{ij}(\mathbf{p}_i, \mathbf{p}_j)$ which depends on their orientations. For simplicity we ignore the effects of non-uniform distributions of motors along microtubules. To linear order in $\Delta\mathbf{v}_{ij}$,

$$\mathbf{F}_{ij} = -\mathbf{G} \cdot [\mathbf{v}_i + s_i\dot{\mathbf{p}}_i + V\mathbf{p}_i - (\mathbf{v}_j + s_j\dot{\mathbf{p}}_j + V\mathbf{p}_j)] \quad (3)$$

where $V\mathbf{p}_i$ is the velocity of the motor relative to the microtubule it is bound to. This choice renders the force between two microtubules dependent on their relative polarities. The linear response coefficient $\mathbf{G}$ is the motor friction and is in general a second rank tensor. In the following we choose $\mathbf{G} = \gamma\mathbf{I}$ for simplicity. For the crosslinking torque we choose $\mathbf{\Gamma}_{ij} = \nu\mathbf{p}_i \times \mathbf{p}_j(\mathbf{p}_i \cdot \mathbf{p}_j)$, which aligns microtubules, as would for instance a torsional stiffness of the crosslinker. The coefficient ν characterizes the magnitude of this effect. It is straightforward to generalize our formulation to include motor activity which varies along the length of a filament, say by pausing at microtubule ends as has been previously argued to drive network contractions [19, 26, 32].

We next derive a continuum theory for our system. We start by expanding Eq. (1) around the center-of-mass positions $\mathbf{x}_i$ and $\mathbf{x}_j$,

$$\mathbf{F}_i = -\gamma L^2 \int_{\Omega(\mathbf{x}_i)} dx^3 \rho(\mathbf{x}) \left[(\mathbf{v}_i - \mathbf{v}(\mathbf{x})) + V(\mathbf{p}_i - \mathbf{P}(\mathbf{x}))\right] - \gamma\frac{L^4}{12} \int_{\Omega(\mathbf{x}_i)} dx^3 \nabla \cdot [\rho(\mathbf{x})(\mathbf{p}_i\dot{\mathbf{p}}_i + \mathcal{H}(\mathbf{x}))] \quad (4)$$

Here we assumed that the length-scale ℓ of gradients in the system is large compared to the microtubule length L and dropped terms with more than one spatial derivative (see Methods). We further introduced the density

$$\rho(\mathbf{x}) = \int d\mathbf{p} \sum_i \delta(\mathbf{x} - \mathbf{x}_i)\delta(\mathbf{p} - \mathbf{p}_i), \quad (5)$$

the polarity $\mathbf{P}(\mathbf{x}) = \langle\mathbf{p}_i\rangle$,

the rotation rate tensor $\mathcal{H}(\mathbf{x}) = \langle\mathbf{p}_i\dot{\mathbf{p}}_i\rangle$ and the velocity field $\mathbf{v}(\mathbf{x}) = \langle\mathbf{v}_i\rangle$, where the angled brackets $\langle\ldots\rangle = 1/\rho \int d\mathbf{p} \sum_i \delta(\mathbf{x} - \mathbf{x}_i)\delta(\mathbf{p} - \mathbf{p}_i)\ldots$ denote local averaging.

The force balance Eq. (2) becomes

$$\nabla \cdot \mathbf{\Sigma}(\mathbf{x}) = - \gamma L^2 \int_{\Omega(\mathbf{x})} dy^3 \rho(\mathbf{x})\rho(\mathbf{y}) \left\{\mathbf{v}(\mathbf{y}) - \mathbf{v}(\mathbf{x}) + V\left(\mathbf{P}(\mathbf{y}) - \mathbf{P}(\mathbf{x})\right)\right\} - \gamma\frac{L^4}{12} \int_{\Omega(\mathbf{x})} dy^3 \rho(\mathbf{x}) \left(\nabla \cdot (\rho(\mathbf{y})\mathcal{H}(\mathbf{y})) + (\nabla\rho(\mathbf{y})) \cdot \mathcal{H}(\mathbf{x})\right). \quad (6)$$

Now, using that $R/\ell \ll 1$ we expand the integrand in Eq. (6) around $\mathbf{x}$ and perform the integration. In this way we obtain for the gel stress

$$\mathbf{\Sigma} = \eta\rho^2(\nabla\mathbf{v} + V\nabla\mathbf{P}) - \alpha\rho^2\mathcal{H}. \quad (7)$$

The coefficients $\eta = \gamma\frac{4\pi}{15}L^2R^5$ and $\alpha = \gamma\frac{4\pi}{36}L^4R^3$ have dimensions of viscosity by density squared. The first term of the stress tensor in Eq. (7) is viscous-like (i.e. depends on $\nabla\mathbf{v}$) and captures long ranged coupling between microtubules. In contrast to a dilute suspension theory, in which a viscous coupling would be induced by the fluid, here it is induced by the crosslinkers. For active crosslinkers ($V \neq 0$) the stress-free state is self-straining and the gel's spontaneous strain rate is $\nabla\mathbf{v} = -V\nabla\mathbf{P}$. The second term of Eq. (7) is generated by microtubules reorienting in the gel and is analogous to a nematic alignment stress in a liquid crystal theory [38]. From Eq. (4), using $\nabla \cdot \mathbf{\Sigma} = 0$, we obtain the flux balance of microtubules

$$\mathbf{v}_i - \mathbf{v} = -V(\mathbf{p}_i - \mathbf{P}) - \frac{L^2}{12}\frac{\nabla\rho}{\rho} \cdot (\mathbf{p}_i\dot{\mathbf{p}}_i - \mathcal{H}). \quad (8)$$

An analogous calculation for the torque balance (see Methods) yields

$$\alpha\mathbf{p}_i \times \dot{\mathbf{p}}_i = \hat{\nu}\mathbf{p}_i \times (\mathbf{p}_i \cdot \mathcal{Q}), \quad (9)$$

which is reminiscent of Maier-Saupe theory and where $\hat{\nu} = \nu L^2 \frac{4\pi R^3}{3}$ and $\mathcal{Q}(\mathbf{x}) = \langle \mathbf{p}_i \mathbf{p}_i \rangle$ is the nematic tensor order parameter. The force balance $\nabla \cdot \mathbf{\Sigma} = \mathbf{0}$ with Eqs. (7,8,9), fully specify the system's dynamics and can be used to time evolve the distribution of microtubule positions and orientations.

Comparison and interpretation. We next use this theory to investigate microtubule sliding in actively crosslinked networks. Consider a fully aligned gel with all $\mathbf{p}_i = \pm\hat{\mathbf{e}}$, for some unit orientation vector $\hat{\mathbf{e}}$. With this, Eq. (9) yields $\dot{\mathbf{p}}_i = 0$. Thus, the force balance $\nabla \cdot \mathbf{\Sigma} = \mathbf{0}$ and the flux balance Eq. (8) are solved by $\mathbf{v}_i = -V\mathbf{p}_i$, when applying no stress boundary conditions at infinity. This means that all microtubules translate with the motor velocity in the direction of their minus end. The velocities of microtubules are independent of the local polarity and only depend on the sliding velocity of the motors themselves. This phenomenon is explained by motors generating an active strain rate in regions of varying polarity. Thus, microtubules can slide past each other without stressing the material since $\nabla \mathbf{v} = -V\nabla \mathbf{P}$, see Eq. (7). Ultimately, the system consists of two interpenetrating gels of microtubules of opposite polarity that push off of each other, with each gel held together by viscous coupling. This is in contrast to dilute suspensions, in which the mass fluxes of left moving and right moving microtubules locally balance, leading to a strong dependence of sliding speed on local polarity.

Our theory predicts that microtubules in the network slide apart at the same speed as isolated pairs of microtubules, independent of the local polarity, as we observe in our experiments (Fig. 2). This prediction does not depend on any adjustable parameters and arises directly from the form of Eqs. (3,1). In turn, the form of Eq. (3) results from imposing that molecular motors act uniformly along the length of microtubules. Our framework can be extended to investigate microtubule networks crosslinked by motors with different properties. For example, dynein accumulates at microtubule minus ends and clusters those ends together [33], leading to network contractions [26, 32]. This can be implemented in our theory by modifying Eq. (3) to include a preference for binding specific parts of the microtubule, and gives rise to the $\mathcal{Q}$ and ρ dependent active stresses that drive many well studied phenomena in active matter systems.

Polarity independent sliding is also observed in spindles formed in *Xenopus* egg extracts. These spindles consist of an array of microtubules which are anti-parallel near the spindle center and highly polar at the spindle poles [34, 35]. Microtubules in these spindles continually slide toward spindle poles, a motion believed to be driven by the molecular motor kinesin-5 [7]. The speed of microtubule sliding is relatively constant throughout the spindle, particularly so when dynein is inhibited [8, 9], and is approximately equal to the speed that kinesin-5 slides apart pairs of anti-parallel microtubules *in vitro* [36]. Our work suggests that this phenomenon naturally arises if microtubules in the spindle are heavily crosslinked and if kinesin-5 acts uniformly along the length of microtubules. We speculate that spindles are self-straining like the XCTK2-microtubule gel presented here.

Many cytoskeletal networks are heavily crosslinked. For instance, the contractility of actin networks has been explained as emerging from its heavily crosslinked nature [30, 37]. The work presented here is an important step towards predicting the material properties of actively crosslinked materials from the properties of their constituents and will enable the design of actively crosslinked networks from first principles.

Data availability: Figs. (1 and 2) are based on microscopy data. The raw data are available from the authors upon reasonable request.

Author Contributions: SF, MJS and DJN developed the theory. BL, PJF, SEM, CEW and ZD performed experiments and provided materials. SF, BL, DJN, and MJS wrote the paper with input from all authors.

Acknowledgements: CEW acknowledges support by NIH R35GM122482. DJN acknowledges the Kavli Institute for Bionano Science and Technology at Harvard University, and National Science Foundation grants PHY-1305254, PHY-0847188, DMR-0820484, and DBI-0959721. PJF acknowledges the Gordon and Betty Moore Foundation for support as a Physics of Living Systems Fellow through Grant GBMF4513. MJS acknowledges National Science Foundation Grants DMR-0820341 (NYU MRSEC), DMS-1463962, and DMS-1620331. We acknowledge support from the NSF MRSEC DMR-1420382.

[1] MC Marchetti, JF Joanny, S Ramaswamy, TB Liverpool, J Prost, Madan Rao, and R Aditi Simha. Hydrodynamics of soft active matter. *Reviews of Modern Physics*, 85(3):1143, 2013.

[2] Daniel Needleman and Zvonimir Dogic. Active matter at the interface between materials science and cell biology. *Nature Reviews Materials*, 2(9):17048, 2017.

[3] B. Alberts, D. Bray, J. Lewis, M. Raff, K. Roberts, and J.D. Watson. *Molecular Biology of the Cell*. Garland, 4th edition, 2002.

[4] Karsten Kruse, Jean-Francois Joanny, Frank Jülicher, Jacques Prost, and Ken Sekimoto. Generic theory of active polar gels: a paradigm for cytoskeletal dynamics. *The European Physical Journal E*, 16(1):5–16, 2005.

[5] JF Joanny, F Jülicher, K Kruse, and J Prost. Hydrodynamic theory for multi-component active polar gels. *New Journal of Physics*, 9(11):422, 2007.

[6] Frank Jülicher, Stephan W Grill, and Guillaume Salbreux. Hydrodynamic theory of active matter. *Reports on Progress in Physics*, 81(7), 2018.

[7] TJ Mitchison. Mechanism and function of poleward flux in Xenopus extract meiotic spindles. *Philosophical Transactions of the Royal Society of London B: Biological Sci-*

ences, 360(1455):623–629, 2005.

[8] Kendra S Burbank, Timothy J Mitchison, and Daniel S Fisher. Slide-and-cluster models for spindle assembly. *Current Biology*, 17(16):1373–1383, 2007.

[9] Ge Yang, Lisa A Cameron, Paul S Maddox, Edward D Salmon, and Gaudenz Danuser. Regional variation of microtubule flux reveals microtubule organization in the metaphase meiotic spindle. *The Journal of Cell Biology*, 182(4):631–639, 2008.

[10] Sundar Ram Naganathan, Sebastian Fürthauer, J. Rodriguez, B. T. Fievet, Frank Jülicher, J. Ahringer, C. V. Cannistraci, and S.W. Grill. Morphogenetic degeneracies in the actomyosin cortex. *Elife*, 7:e37677, 2018.

[11] Johanna Roostalu, Jamie Rickman, Claire Thomas, François Nédélec, and Thomas Surrey. Determinants of polar versus nematic organization in networks of dynamic microtubules and mitotic motors. *Cell*, 175(3):796–808, 2018.

[12] Dennis Bray. Cell movements: from molecules to motility, 2001.

[13] S Fürthauer, M Strempel, SW Grill, and F Jülicher. Active chiral fluids. *The European Physical Journal. E, Soft matter*, 35:89, 2012.

[14] Sumesh P Thampi, Ramin Golestanian, and Julia M Yeomans. Velocity correlations in an active nematic. *Physical Review Letters*, 111(11):118101, 2013.

[15] Guillaume Salbreux, Jacques Prost, and Jean-Francois Joanny. Hydrodynamics of cellular cortical flows and the formation of contractile rings. *Physical Review Letters*, 103(5):058102, 2009.

[16] Mirjam Mayer, Martin Depken, Justin S Bois, Frank Jülicher, and Stephan W Grill. Anisotropies in cortical tension reveal the physical basis of polarizing cortical flows. *Nature*, 467(7315):617–621, 2010.

[17] Sundar Ram Naganathan, Sebastian Fürthauer, Masatoshi Nishikawa, Frank Jülicher, and Stephan W Grill. Active torque generation by the actomyosin cell cortex drives left–right symmetry breaking. *Elife*, 3:e04165, 2014.

[18] Jan Brugués and Daniel Needleman. Physical basis of spindle self-organization. *Proceedings of the National Academy of Sciences*, 111(52):18496–18500, 2014.

[19] Karsten Kruse and F Jülicher. Actively contracting bundles of polar filaments. *Physical Review Letters*, 85(8):1778, 2000.

[20] Igor S Aranson and Lev S Tsimring. Pattern formation of microtubules and motors: Inelastic interaction of polar rods. *Physical Review E*, 71(5):050901, 2005.

[21] Tanniemola B Liverpool and M Cristina Marchetti. Bridging the microscopic and the hydrodynamic in active filament solutions. *EPL (Europhysics Letters)*, 69(5):846, 2005.

[22] Tanniemola B Liverpool and M Cristina Marchetti. Hydrodynamics and rheology of active polar filaments. In *Cell Motility*, pages 177–206. Springer, 2008.

[23] David Saintillan and Michael J Shelley. Instabilities and pattern formation in active particle suspensions: kinetic theory and continuum simulations. *Physical Review Letters*, 100(17):178103, 2008.

[24] David Saintillan and Michael J Shelley. Instabilities, pattern formation, and mixing in active suspensions. *Physics of Fluids*, 20(12):123304, 2008.

[25] David Saintillan and Michael J Shelley. Active suspensions and their nonlinear models. *Comptes Rendus Physique*, 14(6):497–517, 2013.

[26] Peter J Foster, Sebastian Fürthauer, Michael J Shelley, and Daniel J Needleman. Active contraction of microtubule networks. *eLife*, page e10837, 2015.

[27] Tong Gao, Robert Blackwell, Matthew A. Glaser, M. D. Betterton, and Michael J. Shelley. Multiscale polar theory of microtubule and motor-protein assemblies. *Phys. Rev. Lett.*, 114:048101, Jan 2015.

[28] Sebastian Heidenreich, Jörn Dunkel, Sabine HL Klapp, and Markus Bär. Hydrodynamic length-scale selection in microswimmer suspensions. *Physical Review E*, 94(2):020601, 2016.

[29] Ivan Maryshev, Davide Marenduzzo, Andrew B Goryachev, and Alexander Morozov. Kinetic theory of pattern formation in mixtures of microtubules and molecular motors. *Physical Review E*, 97(2):022412, 2018.

[30] Julio M Belmonte, Maria Leptin, and François Nédélec. A theory that predicts behaviors of disordered cytoskeletal networks. *Molecular Systems Biology*, 13(9):941, 2017.

[31] Christian Hentrich and Thomas Surrey. Microtubule organization by the antagonistic mitotic motors kinesin-5 and kinesin-14. *The Journal of Cell Biology*, 189(3):465–480, 2010.

[32] Peter J Foster, Wen Yan, Sebastian Fürthauer, M Shelley, and Daniel J Needleman. Connecting macroscopic dynamics with microscopic properties in active microtubule network contraction. *New Journal of Physics*, 19(12):125011, 2017.

[33] Ruensern Tan, Peter J Foster, Daniel J Needleman, and Richard J McKenney. Cooperative accumulation of dynein-dynactin at microtubule minus-ends drives microtubule network reorganization. *Developmental Cell*, 44(2):233–247, 2018.

[34] Jan Brugués, Valeria Nuzzo, Eric Mazur, and Daniel J Needleman. Nucleation and transport organize microtubules in metaphase spindles. *Cell*, 149(3):554–564, 2012.

[35] Che-Hang Yu, Noah Langowitz, Hai-Yin Wu, Reza Farhadifar, Jan Brugues, Tae Yeon Yoo, and Daniel Needleman. Measuring microtubule polarity in spindles with second-harmonic generation. *Biophysical Journal*, 106(8):1578–1587, 2014.

[36] Lukas C Kapitein, Erwin JG Peterman, Benjamin H Kwok, Jeffrey H Kim, Tarun M Kapoor, and Christoph F Schmidt. The bipolar mitotic kinesin eg5 moves on both microtubules that it crosslinks. *Nature*, 435(7038):114, 2005.

[37] Pierre Ronceray, Chase P Broedersz, and Martin Lenz. Fiber networks amplify active stress. *Proceedings of the National Academy of Sciences*, 113(11):2827–2832, 2016.

[38] We note the ordering stress recovers the form derived for kinetic theories that approximate microtubule alignment by the Maier-Saupe free-energy [25] when using Eq. (9).

arXiv:1812.01079v1 [cond-mat.soft] 3 Dec 2018

Methods

I. EXPANSION OF THE MICROTUBULE FORCE BALANCE

In the following, we illustrate in more detail how Eq. (**??**) is expanded to obtain Eq. (**??**). We start by rewriting Eq. (**??**) in terms of variables rescaled to the system size ℓ, and inserting the force velocity relation Eq. (**??**).

$$\mathbf{F}_i \;=\; -\gamma\ell^6 \int_{\hat{L}/2}^{-\hat{L}/2} d\hat{s}_i \sum_j \int_{\hat{L}/2}^{-\hat{L}/2} d\hat{s}_j \int d\mathbf{p} \int_{\hat{\Omega}(\ell(\hat{\mathbf{x}}_\mathbf{i}+\hat{s}_i\mathbf{p}_i))} d\hat{x}^3 \left\{\delta(\ell(\hat{\mathbf{x}}-\hat{\mathbf{x}}_\mathbf{j}-\hat{s}_j\mathbf{p}_\mathbf{j})\hat{\mathbf{F}}_{ij}\right\}, \tag{S.I-1}$$

where we introduced the length rescaled variables $\ell\hat{x} = x$. Most importantly the rescaled microtubule length $\hat{L} = L/\ell$ and the force $\hat{\mathbf{F}}_{ij} = \mathbf{F}_{ij}/\ell$. We next expand the argument of the integral by writing

$$\delta(\ell(\hat{\mathbf{x}}-\hat{\mathbf{x}}_j-\hat{s}_j\mathbf{p}))\hat{\mathbf{F}}_{ij} = \delta(\ell(\hat{\mathbf{x}}-\hat{\mathbf{x}}_j))\hat{\mathbf{F}}_{ij} - \ell\hat{s}_j\mathbf{p}_j\cdot\nabla\delta(\ell(\hat{\mathbf{x}}-\hat{\mathbf{x}}_j))\hat{\mathbf{F}}_{ij} + \mathbf{O}(\varepsilon^3) \tag{S.I-2}$$

where we use that $\hat{s}_j$ and $\hat{\mathbf{F}}_{ij}$ are small quantities of order ε. Then Eq. S.I-2 becomes,

$$\begin{aligned}\mathbf{F}_i \;=\; -\gamma\ell^6 \int_{\hat{L}/2}^{-\hat{L}/2} d\hat{s}_i \sum_j \int_{\hat{L}/2}^{-\hat{L}/2} d\hat{s}_j \int d\mathbf{p} \int_{\hat{\Omega}(\ell(\hat{\mathbf{x}}_\mathbf{i}+\hat{s}_i\mathbf{p}_i))} d\hat{x}^3 \left\{\delta(\ell(\hat{\mathbf{x}}-\hat{\mathbf{x}}_\mathbf{j})\left(\hat{\mathbf{F}}_{ij} - \ell\hat{s}_j\nabla\cdot\mathbf{p}_j\hat{\mathbf{F}}_{ij}\right)\right\} \\ +\mathcal{O}(\varepsilon^8),\end{aligned} \tag{S.I-3}$$

where we used that $\int_{\hat{\Omega}} d\hat{x}^3 \simeq \varepsilon^3$. We next use that

$$\int_{\hat{\Omega}(\ell(\hat{\mathbf{x}}_i+\hat{s}_i\mathbf{p}_\mathbf{i}))} d\hat{x}^3 X = \int_{\hat{\Omega}(\ell(\hat{\mathbf{x}}))} d\hat{x}^3 \left(X + \ell\nabla\cdot\hat{s}_i\mathbf{p}_\mathbf{i}X\right) + \mathcal{O}(\varepsilon^5 X) \tag{S.I-4}$$

and finally find

$$\begin{aligned}\mathbf{F}_i \;=\; -\gamma\ell^6 \int_{\hat{L}/2}^{-\hat{L}/2} d\hat{s}_i \sum_j \int_{\hat{L}/2}^{-\hat{L}/2} d\hat{s}_j \int d\mathbf{p} \int_{\hat{\Omega}(\ell(\hat{\mathbf{x}}_\mathbf{i}))} d\hat{x}^3 \left\{\delta(\ell(\hat{\mathbf{x}}-\hat{\mathbf{x}}_\mathbf{j})\left(\hat{\mathbf{F}}_{ij} - \ell\nabla\cdot\left(\hat{s}_j\mathbf{p}_j - \hat{s}_i\mathbf{p}_i\right)\hat{\mathbf{F}}_{ij}\right)\right\} \\ +\mathcal{O}(\varepsilon^8),\end{aligned} \tag{S.I-5}$$

executing the integrals over $\hat{s}_i, \hat{s}_j$ and returning to natural variables yields Eq. (**??**).

II. TORQUE BALANCE

In this section we derive equation (**??**) from the total torque

$$\mathbf{T}_i = \int_{-L/2}^{L/2} ds_i \sum_j \int_{-L/2}^{L/2} ds_j \int d\mathbf{p} \int_{\Omega(\mathbf{x}_i+s_i\mathbf{p}_i)} dx^3 \left\{\delta(\mathbf{x}-\mathbf{x}_j-s_j\mathbf{p}_j)\delta(\mathbf{p}-\mathbf{p}_j)\mathbf{T}_{ij}\right\} = 0, \tag{S.II-1}$$

on the i-th microtubule. We start by rewriting (S.II-1) using $\mathbf{\Gamma}_{ij} = \nu\mathbf{p}_i\times\mathbf{p}_j(\mathbf{p}_i\cdot\mathbf{p}_j)$ and the expression for $\mathbf{F}_{ij}$ from Eq. (**??**),

$$\begin{aligned}\mathbf{T}_i^{(0)} \;=\; -\gamma\mathbf{p}_i\times \int_{-L/2}^{L/2} ds_i \sum_j \int_{-L/2}^{L/2} ds_j \int d\mathbf{p} \int_{\Omega(\mathbf{x}_i+s_i\mathbf{p}_i)} dx^3 \\ \left\{s_i\delta(\mathbf{x}-\mathbf{x}_j-s_j\mathbf{p}_j)\delta(\mathbf{p}-\mathbf{p}_j)\;\left(\mathbf{v}_i+s_i\mathbf{p}_i-\mathbf{v}_j-s_j\mathbf{p}_j-V\mathbf{p}_j\right)\right\}\end{aligned} \tag{S.II-2}$$

where we used $\mathbf{p}_i \times \mathbf{p}_i = 0$ and

$$\mathbf{T}_i^{(1)} = \int_{-L/2}^{L/2} ds_i \int_{-L/2}^{L/2} ds_j \int d\mathbf{p} \int_{\Omega(\mathbf{x}_i + s_i \mathbf{p}_i)} dx^3 \left\{ \mathbf{p}_i \times \mathbf{p}_j (\mathbf{p}_i \cdot \mathbf{p}_j) \right\}. \tag{S.II-3}$$

For notational convenience we separated the total MT torque $\mathbf{T}_i = \mathbf{T}_i^{(0)} + \mathbf{T}_i^{(1)}$ into parts generated by crosslinking forces $\mathbf{T}_i^{(0)}$ and by crosslinking torques $\mathbf{T}_i^{(1)}$. From here we follow the expansion steps outlined for the force balance in the main text and obtain

$$\mathbf{T}_i^{(0)} = -\gamma \frac{L^4}{12} \int_{\Omega(\mathbf{x}_i)} dx^3 \rho(\mathbf{x}) \mathbf{p}_i \times \dot{\mathbf{p}}_i - \gamma \frac{L^4}{12} (\mathbf{p}_i \cdot \nabla) \mathbf{p}_i \times \int_{\Omega(\mathbf{x}_i)} dx^3 \rho(\mathbf{x}) \left(\mathbf{v}_i - \mathbf{v}(\mathbf{x}) - V \mathbf{P}(\mathbf{x}) \right). \tag{S.II-4}$$

and

$$\mathbf{T}_i^{(1)} = \rho \hat{\nu} \mathbf{p}_i \times (\mathbf{p}_i \cdot \mathcal{Q}), \tag{S.II-5}$$

with $\hat{\nu} = \nu L^2 \frac{4\pi R^3}{3}$. To simplify this expression consider

$$\begin{aligned} & \mathbf{p}_i \times [\mathbf{v}_i - \mathbf{v}(\mathbf{x}) - V P(\mathbf{x})] \\ = \; & \mathbf{p}_i \times [\mathbf{v}_i - \mathbf{v}(\mathbf{x}_i) + V(\mathbf{p}_i - \mathbf{P}(\mathbf{x}_i)) + (\mathbf{v}(\mathbf{x}_i) - \mathbf{v}(\mathbf{x}) + V(P(\mathbf{x}_i) - P(\mathbf{x})))] \\ = \; & \mathbf{p}_i \times [-\frac{L^2}{12} \frac{\nabla \rho}{\rho} \cdot (\mathbf{p}_i \dot{\mathbf{p}}_i - \mathcal{H}) + (\mathbf{v}(\mathbf{x}_i) - \mathbf{v}(\mathbf{x}) + V(P(\mathbf{x}_i) - P(\mathbf{x})))], \end{aligned} \tag{S.II-6}$$

where we used Eq.(**??**). After inserting Eq. (S.II-6) back into Eq. (S.II-4) and using the force balance equation (**??**) we finally obtain

$$\alpha \rho \left(1 - \frac{L^2}{12} \left(\mathbf{p}_i \cdot \nabla \frac{\mathbf{p}_i \cdot \nabla \rho}{\rho} \right) \right) \mathbf{p}_i \times \dot{\mathbf{p}}_i = \rho \hat{\nu} \mathbf{p}_i \times (\mathbf{p}_i \cdot \mathcal{Q}) + \alpha \frac{L^2}{12} (\mathbf{p}_i \cdot \nabla) \mathbf{p}_i \times \nabla \cdot (\rho \mathcal{H}), \tag{S.II-7}$$

which becomes Eq. (**??**) after dropping higher order terms.

III. EXPERIMENTAL PROCEDURE

To study the behavior of highly crosslinked active gels we performed experiments on an *in vitro* system of purified components. We made solutions of tubulin and mCitrine-XCTK2, a Kinesin-14 molecular motor capable of crosslinking and sliding aligned microtubules. To image the tubulin, it was fluorescently labeled with 0.7% of Atto 565 NHS-Ester. We then added paclitaxel, which nucleates and stabilizes microtubules; and rapidly loaded the sample into a thin rectangular microfluidic chamber with approximate dimensions of $0.1 \times 1 \times 20\text{mm}^3$. The microtubule-motor mixture spontaneously self-organized into a highly aligned macroscopic gel, oriented along the long axis of the microfluidic channel (Fig. **??** A).

We photo-bleached fluorescent microtubules with lines perpendicular to the axis of gel alignment (see Imaging and Bleaching section of SI). Photobleaching bleached the Atto 565 labeled microtubules, but did not change the structure of the co-located mCitrine-XCTK2 as seen in Supplementary (Fig. 1), demonstrating that the photobleaching did not ablate the microtubules. As bleaching marks a subset of microtubules, it allows their subsequent motions to be monitored. We observe that bleached lines split into two, and this subsequent pair of lines moved apart along the direction of nematic alignment (Fig. **??** B, left), indicating that microtubules in the gel are continually sliding relative to each other.

IV. CLONING, EXPRESSION AND PURIFICATION OF MCIT-XCTK2

Full-length amino-terminally tagged mCitrine XCTK2 (mCit-XCTK2) was expressed in and purified from baculovirus infected Sf-9 cells (Invitrogen) using conventional chromatography as previously described[S1]. Baculovirus stocks were created from pFB-mCit-XCTK2 using the Bac-to-Bac System (Invitrogen). pFB-mCit-XCTK2 was created from pFB-mCit-DEST[S2] and pENTR-XCTK2 using the Gateway System. The full-length coding sequence of XCTK2 was amplified by PCR and inserted into pENTR using the pENTR/D-TOPO kit (Invitrogen) to create pENTR-XCTK2. The plasmids are available from the authors upon reasonable request.

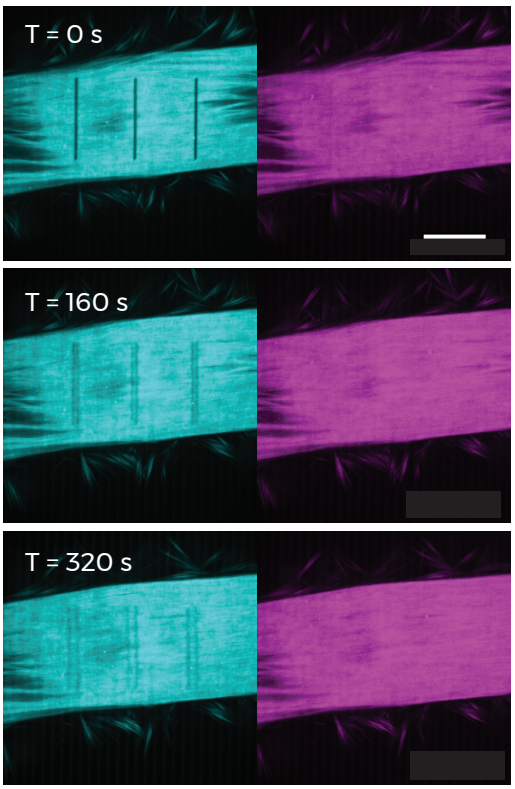


FIG. 1: Photo-bleached lines label the Atto 565 labeled microtubules (Cyan, Left), but do not change the structure of the co-located mCitrine-XCTK2 (Magenta, Right). Scale bar is 100 μm.

V. CHAMBER FABRICATION

Imaging chambers consisting of a slide and coverslip with a 0.9mm channel in a 110μm PDMS spacer. Briefly, masters were made by first covering a slide with polyester film (Schein Holographics) to prevent PDMS adhesion. A 0.9mm $\times$ 47.5mm rectangle was cut from adhesive vinyl (3M Gerber InstaChange) using a die cutter (Silhouette Cameo), and adhered to the polyester coated slide. PDMS (Dow Corning, 1:10 mixing ratio) was poured over the master and degassed before a second, uncoated, slide was placed on top and secured in place using binder clips. Sandwiched slides were baked overnight at 60°C. The slides were then separated, leaving a slide with adhered PDMS and the polyester coated slide, which was discarded. The PDMS coated slide and an 18mm $\times$ 18mm coverslip were each treated with air plasma for 1 minute using a corona device before bonding. Chambers were loaded with passivation mix consisting of 5mg/mL BSA (JT Baker) and 5% (w/v) Pluronic F-127 (Sigma P2443) and incubated overnight at 8°C. Before use, passivation mix was flushed from the chambers using BRB80.

VI. SELF-ORGANIZATION ASSAY

Self-organization buffer (SOB) was adapted from (Hentrich 2010) [S3] and prepared as a 2x stock containing 40 mM PIPES (Sigma P6757), 2mM EGTA (Sigma E4378), 14.5mM MgCl2 (Sigma M8266), 10mM ATP (Sigma A2383), 3mM GTP (Sigma G8877), 2mM β-mercaptoethanol (Bio-Rad #161-0710), 100mM KCl (Sigma 60130), 400mM Sucrose (Sigma 84097), 61.5mM Glucose (Sigma D9434), pH 6.85. Reaction mix consisting of 10 μL 2x SOB, 0.6μL Gloxy, 1 μL mCit-XCTK2 (10 μM stock), 0.7 μL PK/LDH (Sigma P0294), 0.5 μL PEP (MP Biomedicals, IC15187280), 4.15 μL Milli-Q H_2O, and 0.25μL Atto-565 labeled tubulin (20 μM stock) and 2.32 μL unlabeled tubulin (300μM stock). Reactions were initiated by the addition of 0.4 μL paclitaxel (Sigma T7191, 100 μM stock). Immediately after paclitaxel addition, the reaction mix was loaded into a passivated imaging chamber, and the chamber inlet and outlet were sealed using candle wax.

We estimate the initial concentration of tubulin to be 36 μM. We estimate from confocal data with slices taken

every 3μm that the material contracts to 24 μm in height and 200 μm in width. We also estimate from taking background florescence data that roughly 25% of the tubulin remains outside the contracting network. This back of the envelope calculation gives a tubulin concentration in the final state to be 558 μM. Based off previous MT length distribution measurements in similar experiments [S4] suggesting that the microtubules will be very roughly 6 μm , we can estimate that there are 20,000 tubulin units per microtubule. This gives a number concentration of 27.9 nM microtubules, or 1.7×10^{10} microtubules per μL. Given the 25 nm diameter of a microtubule and the estimated length, this results in a volume fraction of 5%. Since there are 17 microtubules per μm^3, we estimate that the average distance between microtubules is 389 nm.

VII. IMAGING AND BLEACHING

The imaging system consists of an inverted microscope (Eclipse Ti, Nikon), with a femtosecond Ti:sapphire pulsed laser (Mai-Tai, Spectra-Physics) for excitation (800 nm wavelength, 80 MHz repetition rate, 70 fs pulse width), a commercial scanning system (DCS-120, Becker & Hickl), and hybrid detectors (HPM-100-40, Becker & Hickl). The excitation laser was collimated by a telescope to avoid any power loss at the XY galvanometric mirror scanner and to fill the back aperture of a water-immersion objective (CFI Apo 40 WI, NA 1.25, Nikon).

Two-photon fluorescence was imaged with an emission filter wheel controlled by μManager (Edelstein et al., 2014) that contained filters for mCitrine-labels on XCTK2 (FF01-510/42-25, Semrock) and Atto565-labeled tubulin (FF01-607/36-25, Semrock). The optical path contained a short-pass filter (FF01-650/SP-25, Semrock) to block the fundamental laser wavelength. Samples were imaged at room temperature ($\simeq 21°$C).

During imaging signal was acquired for 10 s of integration time at a spatial resolution of 512x512 pixels over a 110x110 μm^2 field of view. The maximum scan rate of the DCS-120 at this resolution is 2 frames/s. The power of the excitation laser was adjusted to 10 mW at the objective.

To bleach, the excitation laser was adjusted to 40 mW as measured at the objective. The spatial resolution was decreased to 16x16 pixels over a 440x440 μm^2 field of view. A 30s scan at this resolution results in 16 distinct bleached lines at the wider FoV, and 4 distinct lines in the smaller FoV used for imaging.

Subsequent experiments to investigate possible three-dimensional considerations of the material was performed using the same laser attached to a Spinning Disk confocal microscope. This data was acquired on an EMCCD camera of 512 512 pixels (ImageM enhanced C9100-13; Hamamatsu Photonics). The images were using μManager software (Vale laboratory at University of California, San Francisco) and Z-stack images were acquired by high-speed piezo-Z scanner (P-725 PIFOC; Physik Instrumente).

VIII. DATA ANALYSIS

Fluorescence image data was manually cropped to include just one splitting line. A temporal series of cropped images was read into Matlab for analysis. Data was binned in the direction parallel to the bleach lines and fitted by a function of two Gaussian functions plus a linear slope. A linear fit of the temporal series of the location of the Gaussian functions was used to calculate relative velocities between the two Gaussian functions. The amplitudes of the Gaussian functions, A_1 and A_2, were used to calculate experimental polarity as $P_{exp} = |\frac{A_1 - A_2}{A_1 + A_2}|$. This code has been made publicly available at `https://github.com/bezlemma`

[S1] Claire E Walczak, Suzie Verma, and Timothy J Mitchison. Xctk2: a kinesin-related protein that promotes mitotic spindle assembly in xenopus laevis egg extracts. *The Journal of Cell Biology*, 136(4):859–870, 1997.

[S2] Stephanie C Ems-McClung, Sarah G Hainline, Jenna Devare, Hailing Zong, Shang Cai, Stephanie K Carnes, Sidney L Shaw, and Claire E Walczak. Aurora b inhibits mcak activity through a phosphoconformational switch that reduces microtubule association. *Current Biology*, 23(24):2491–2499, 2013.

[S3] Christian Hentrich and Thomas Surrey. Microtubule organization by the antagonistic mitotic motors kinesin-5 and kinesin-14. *The Journal of Cell Biology*, 189(3):465–480, 2010.

[S4] Peter J Foster, Wen Yan, Sebastian Fürthauer, M Shelley, and Daniel J Needleman. Connecting macroscopic dynamics with microscopic properties in active microtubule network contraction. *New Journal of Physics*, 19, 2017.